

ARTICLE OPEN



Global increase in future compound heat stress-heavy precipitation hazards and associated socio-ecosystem risks

Zhiling Zhou¹, Liping Zhang^{1,2,✉}, Qin Zhang^{1,3}, Chen Hu^{1,2,✉}, Gangsheng Wang^{1,2}, Dunxian She^{1,2} and Jie Chen^{1,2}

Compound extremes of lethal heat stress-heavy precipitation events (CHPEs) seriously threaten social and ecological sustainability, while their evolution and effects at the global scale under climate warming remain unclear. Here we develop the global picture of projected changes in CHPEs under various scenarios and investigate their socioeconomic and ecosystem risks combining hazard, exposure, and vulnerability through the composite indicator approach. We find a high percentage of heat stress is followed by heavy precipitation, probably driven by atmospheric conditions. Global average frequency and intensity of CHPEs are projected to increase in the future under high-emission scenarios. Joint return periods of CHPEs are projected to decrease globally, predominantly driven by changes in heat stress extremes. In the long-term future, over half of the population, gross domestic product, and gross primary productivity may face high risk in most regions, with developed regions facing the highest risks under SSP5-8.5 and developing regions facing the highest risks under SSP3-7.0.

npj Climate and Atmospheric Science (2024)7:33; <https://doi.org/10.1038/s41612-024-00579-4>

INTRODUCTION

Heat stress (HS) and heavy precipitation (PR) are two of the most hazardous climate extremes, posing serious threats to human health, sustainable development, and ecological security^{1–3}. The increasing sensible heat and moisture in the low atmosphere during HS may set the stage for PR⁴, leading to the occurrence of compound heat stress and heavy precipitation events (CHPEs). It is well-established that compound climate extreme events can have even more devastating consequences compared to individual extremes^{5–8}. For example, an HS event closely followed by heavy rainfall caused the deaths of more than 500,000 livestock and over \$1.2 billion in economic losses in Queensland, Australia, in February 2019⁴. Recent research efforts have been devoted towards investigating the occurrence of regional compound heatwave and precipitation events. You and Wang⁹ observed that 22% of land areas experienced statistically significant consecutive heatwave and heavy rainfall events within 7 days in China during the 1981–2005 period. Ning et al.¹⁰ reported that approximately one-quarter of summer precipitation extremes in China, particularly in western regions, were preceded by extreme heat events. In the central United States, a significant percentage of floods were also found to be preceded by heat stress events⁴. Nevertheless, it remains a continued challenge to adequately describe CHPEs, particularly in terms of establishing a comprehensive and universally applicable index. Moreover, these studies only focus on historical periods and specific regions. The global hotspots of CHPEs and their evolutions remain unclear.

Global warming has substantially altered the frequency and intensity of HWs and PRs at regional and global scales^{5,6}. Furthermore, the dependence between temperature and precipitation is projected to increase, particularly in the Northern Hemisphere¹¹, possibly leading to an increase in the probability of CHPEs. To facilitate adaptation and mitigation strategies, it is important to project the future evolution of CHPE characteristics, hazards, and further risks in a warming climate. Recently, Ren

et al.⁷ projected the spatiotemporal variations of compound heatwave and heavy precipitation (CHWHP) events in Guangdong, China under two SSPs. However, the intensity of CHWHPs in their study was solely based on temperature, without considering the precipitation during the compound events. At the global scale, although no previous study has explored the CHPEs, we notice that Gu et al.⁸ investigated the compound flood-hot (CFH) extremes in catchments over the globe under the combined scenarios of Representative Concentration Pathways (RCPs) and Shared Socioeconomic Pathways (SSPs), and found the joint return periods (JRP) of CFHs are projected to decrease globally. Nevertheless, there is no sequential relationship between flood and heatwave events in their study, and the physical connection between high temperature and flood is weaker than that between heat stress and heavy rainfall. Moreover, the heatwaves in these two studies are simply defined using the daily maximum temperature, whereas the lethality of heatwave events depends not only on high temperature but also on air humidity¹². Hot and humid environments can reduce the effectiveness of evaporation, which is the primary way of expelling excess heat from the human body, leading to impossible thermoregulation and heat stress/stroke¹³. Numerous indices have been employed to quantify heat stress in previous studies, including apparent temperature¹⁴, US National Oceanic and Atmospheric Administration (NOAA) heat index¹⁵, humidex¹⁶, and wet bulb temperature (T_{WB})¹⁷. Among them, the T_{WB} , which is a weighted mean of the dry bulb, wet bulb, and mean radiant (globe) temperatures, has been widely used in climate impact studies^{4,18,19}. Based on the concept of T_{WB} , Wouters et al.²⁰ defined the lethal heat stress temperature index (T_h) that could better incorporate the relation between heat stress and mortality than T_{WB} when preserving its physical bases.

In addition to investigating the evolution of extreme events, assessing and projecting the risk they pose to society is an important topic in the study of climate impacts and adaptation to climate change. Risk refers to the potential for significant negative

¹State Key Laboratory of Water Resources Engineering and Management, Wuhan University, 430072 Wuhan, People's Republic of China. ²Institute for Water-Carbon Cycles and Carbon Neutrality, Wuhan University, 430072 Wuhan, People's Republic of China. ³Changjiang River Scientific Research Institute of Changjiang Water Resources Commission, 430010 Wuhan, China. ✉email: zhanglp@whu.edu.cn; huchen1996@whu.edu.cn

shifts resulting from the interaction between hazardous climate events and vulnerable social conditions, ultimately leading to widespread adverse impacts within a community or system²¹. Previous studies have projected the future social risk of single climate events^{22–25}, while the future risk for compound events has been barely explored. According to the risk frame proposed by the Intergovernmental Panel on Climate Change (IPCC), risk can be assessed by combining three determinants: hazard, exposure, and vulnerability²¹. The composite indicator approach (CIA) is widely utilized since it can establish standardized evaluation guidelines for impact reduction at both regional and global scales²⁶. Hazard refers to the physical natural events and is always quantified by characteristics of the climate extremes. Exposure is the presence of objects that can be adversely affected, which is normally described by population and gross domestic product (GDP). Vulnerability encompasses the system's propensity to be adversely affected by climate hazards and its ability to withstand and recover from disasters. We choose the cropland and built-up land area and GDP per capita to reflect socioeconomic vulnerability. Moreover, besides calculating the socioeconomic risk of CHPEs, we apply the IPCC risk frame to assess and project the ecological risk in this study as the ecosystem can also be adversely impacted by HS and PR^{27,28}. The gross primary productivity (GPP) is used to reflect ecological exposure here²⁷, and the fragile plant area (i.e., scrub, grass, wetlands, and cropland)²⁹ is used to describe ecological vulnerability.

In this study, we aim to investigate the characteristics and bivariate hazards of CHPEs, as well as their socioeconomic and ecological risk at grid, regional, and global scales, and disentangle how CHPEs and associated risks changed in the past and are likely to change in the future. We utilize both the reanalysis dataset and model simulations from six global climate models (GCMs) in the latest sixth Coupled Model Inter-comparison Project (CMIP6). The CHPEs are defined as the occurrence of HS events followed by PR events within three days. We check the probability of CHPE occurrence using a fraction indicator and assess the physical mechanism behind CHPEs by measuring the responses of large-scale atmospheric dynamics during CHPEs. We define a composite intensity indicator considering both the characteristics of HS and PR events to quantify the spatiotemporal variations of CHPEs. To provide a potential range of future CHPE evolution under varying socioeconomic and emissions scenarios, we then project the CHPEs under four combined SSP-RCP scenarios from CMIP6 (i.e., SSP1-2.6, SSP2-4.5, SSP3-7.0, and SSP5-8.5)^{30,31}. We further disentangle the future changes in bivariate hazards of CHPEs using JRPs under the 'and' hazard scenario and attribute the JRP changes to single HS, PR events, and their dependence by conducting controlled experiments. We introduce a contribution fraction indicator to quantify the proportional impact of the three primary drivers on JRP changes. Moreover, we assess future shifts in the socioeconomic and ecological risks of CHPEs under different scenarios using socioeconomic data, land cover data, and GPP datasets. We finally quantified the exposed population, GDP, and GPP under high risk in 23 IPCC climate regions.

RESULTS

Observed CHPE and atmospheric conditions

Observed daily T_h and precipitation series are positively correlated in most regions around the world during the warm season (Supplementary Fig. 1) except western North America, northern South America, the Mediterranean region, and central Africa (Fig. 1f), probably due to the increasing sensible heat flux and moisture convergence under extreme heat stress^{6,32}. We identify global HS, PR, and CHPE events using reanalysis products for the historical period (1979–2014). To assess the probability of CHPEs occurring either following or preceding individual HS or PR events,

we define the fraction indicator Fr_{HS} (Fr_{PR}) as the total count of CHPEs divided by the total count of single HS (PR) events within a specific year. Global average Fr_{HS} (Fr_{PR}) ranges from 20% to 35% (5% to 20%) during the 1979–2014 period, showing a significantly increasing trend of 0.13% (0.15%) per year (Fig. 1m). In specific regions such as the Arctic, eastern Canada, southern South America, eastern Russia, western and northeastern China, and Southeast Asia, Fr_{HS} exceeds 30% each year (Fig. 1a, b), indicating that a large portion of HS events in these areas are followed by precipitation events within three days. Regions with relatively high Fr_{PR} are located in eastern America, northern and eastern Africa, the Middle East, Mongolia, northern China, and Australia, where more than 10% of PR events in these areas are preceded by HS events. The rising Fr_{HS} and Fr_{PR} indicate that the interdependence between HSs and PRs is growing under climate warming.

During the period from 1979 to 2014, the observed CHPEs show a high frequency in the Arctic region, Canada, central United States, southern South America, northern Europe, eastern Russia, and western and northern China, occurring more than once per year (Fig. 1c). The spatial distribution of CHPE duration exhibits similarity with its frequency (Fig. 1d). Moreover, the spatial distributions of CHPE intensity and magnitude also share the same similarity, with high values observed in the Arctic region, central United States, southern South America, northern Europe, eastern and southern Africa, central Russia, western and northern China, northern India, Pakistan, and Australia (Fig. 1e, f). Furthermore, the frequency, duration, intensity, and magnitude of CHPEs all show a significant increasing trend from 1979 to 2014, with a trend of 0.01, 0.04 days, 0.31, and 0.05 per year, respectively (Fig. 1n–q). The phenomenon of Arctic amplification is obvious across all CHPE characteristics.

To disentangle the physical processes of CHPEs, we diagnose the large-scale atmosphere conditions prior to the PR events to support the link between HS and following PRs. Considering both the thermal and dynamical drivers of PR, we select convective available potential energy (CAPE), specific humidity (SH), surface sensible heat flux (SSHF) vertically integrated moisture convergence (VIMC), and total column water vapor (TCWV) and employ composite analysis to diagnose their anomalies. Since the differences in composite anomalies for the large-scale environmental conditions are not sensitive to the selection of 1, 2, or 3 days prior to the PR events⁴, we calculated the mean anomalies of the atmospheric variables 1 day before the occurrence of PR events in the identified CHPEs. When a HS event occurs, the temperature and humidity are high and the sensible heat increases, leading to an increase in atmospheric instability and consequently high CAPE, which can bridge the HS and PR events^{32,33}. In our study, high CAPE accompanied by high SH and SSHF is found in the Arctic region, southeastern South America, northern Europe, and eastern Asia, which may enhance a high moist convection potential (Fig. 1g–i and Supplementary Fig. 2). Besides the dynamical forces, moisture convergence and atmospheric moisture also play a critical role in modulating precipitation patterns based on the moisture budget. In this study, positive anomalies of VIMC and TCWV are found in almost the entire global land surface except Mediterranean and northern South America, suggesting intensified atmospheric moisture transport, which provides favorable conditions for extreme PRs.

Future spatiotemporal variations in CHPE characteristics

We employ historical CHPE simulations from GCMs for the 1979–2013 period as the reference for future projections (2015–2099). The exclusion of the years 2014 and 2100 is due to the fact that the warm season in the southern hemisphere extends into the following year. On a global average of future Fr_{HS} , the disparities among the four future scenarios exhibit a substantial

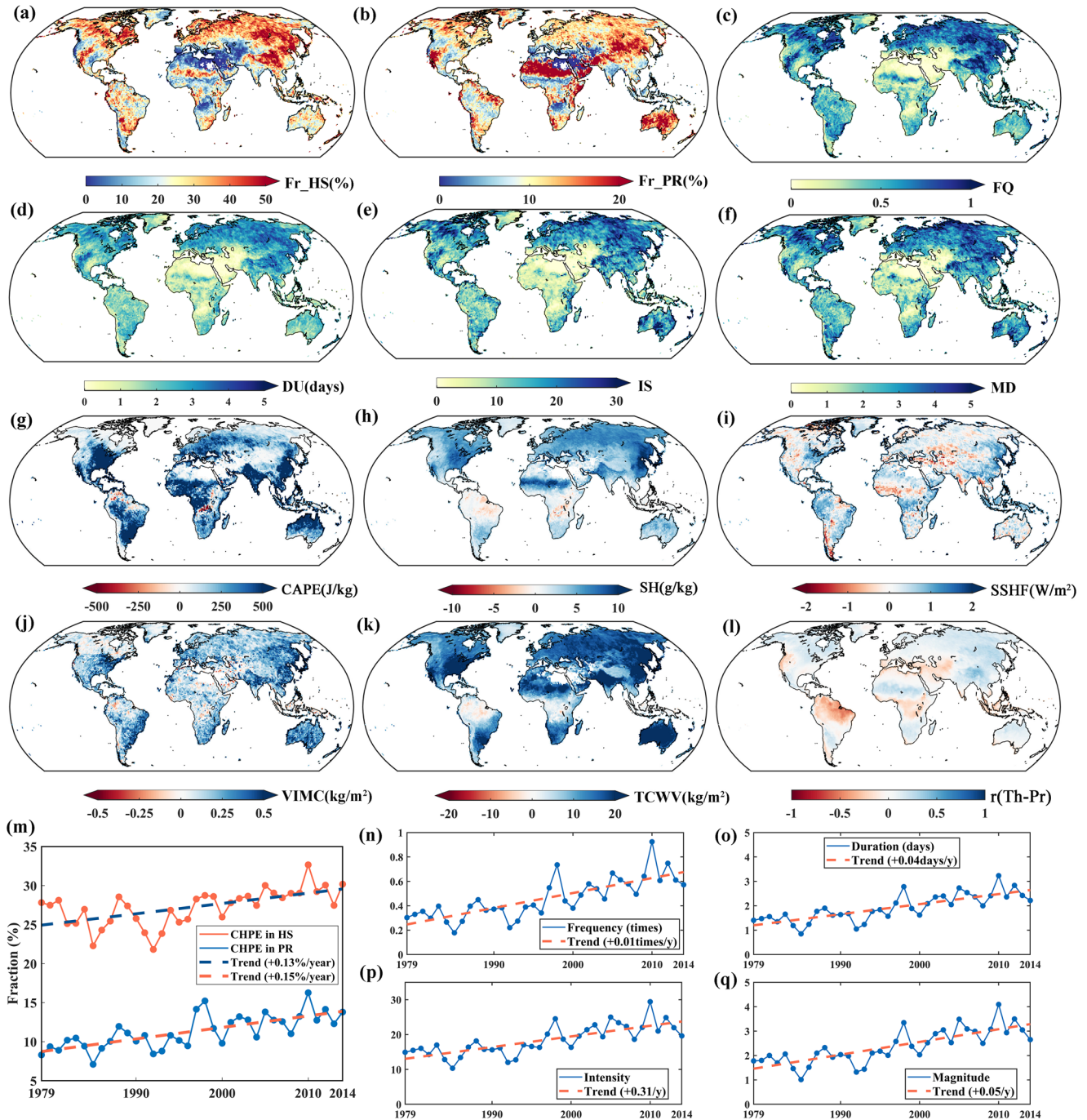


Fig. 1 Observed CHPE characteristics and anomalies of the atmospheric conditions for the historical period (1979–2014). **a, b** Fraction of CHPE in HS (**a**) and PR (**b**) events. **c–f** Observed multi-year average of frequency (**c**), duration (**d**), intensity (**e**), and magnitude (**f**) of CHPE. **g–k** Anomalies of CAPE (**g**), SH (**h**), sensible heat flux (**i**), VIMC (**j**), and TCWV (**k**) during CHPE. **l** Kendall's correlation coefficient (r) between daily T_h and precipitation. **m–q** Temporal changes in the fraction of CHPE in HS and PR (**m**), frequency (**n**), duration (**o**), intensity (**p**), and magnitude (**q**) of CHPE. The trends are estimated by the simple linear regression based on the least squares method, and the significance is evaluated at a 0.05 confidence level by the nonparametric Mann–Kendall trend test.

magnification from 2030 onwards, with higher-emission scenarios exhibiting a greater fraction and larger growth rate. Specifically, the global average Fr_{HS} maintains a robust increasing trend under SSP2-4.5, SSP3-7.0, and SSP5-8.5 throughout the entire future period, while increasing until 2050 and then stabilizes under SSP1-2.6 (Fig. 2i). To clarify the variations of CHPE during different time periods, we divided the future time period into three sub-periods, i.e., near-term (2015–2040), mid-term

(2041–2070), and long-term (2071–2099). The spatial distributions of Fr_{HS} and Fr_{PR} under various scenarios for the three sub-periods are displayed in Fig. 2 and Supplementary Figs. 3 and 4. In the long-term, the global average Fr_{HS} projections reach over 50% under SSP3-7.0 and SSP5-8.5, with more than half of the land areas exceeding 70%, which suggests a substantial portion of HS events is closely followed by PR events. Regarding spatial distribution, there are notable differences in Fr_{HS} across different

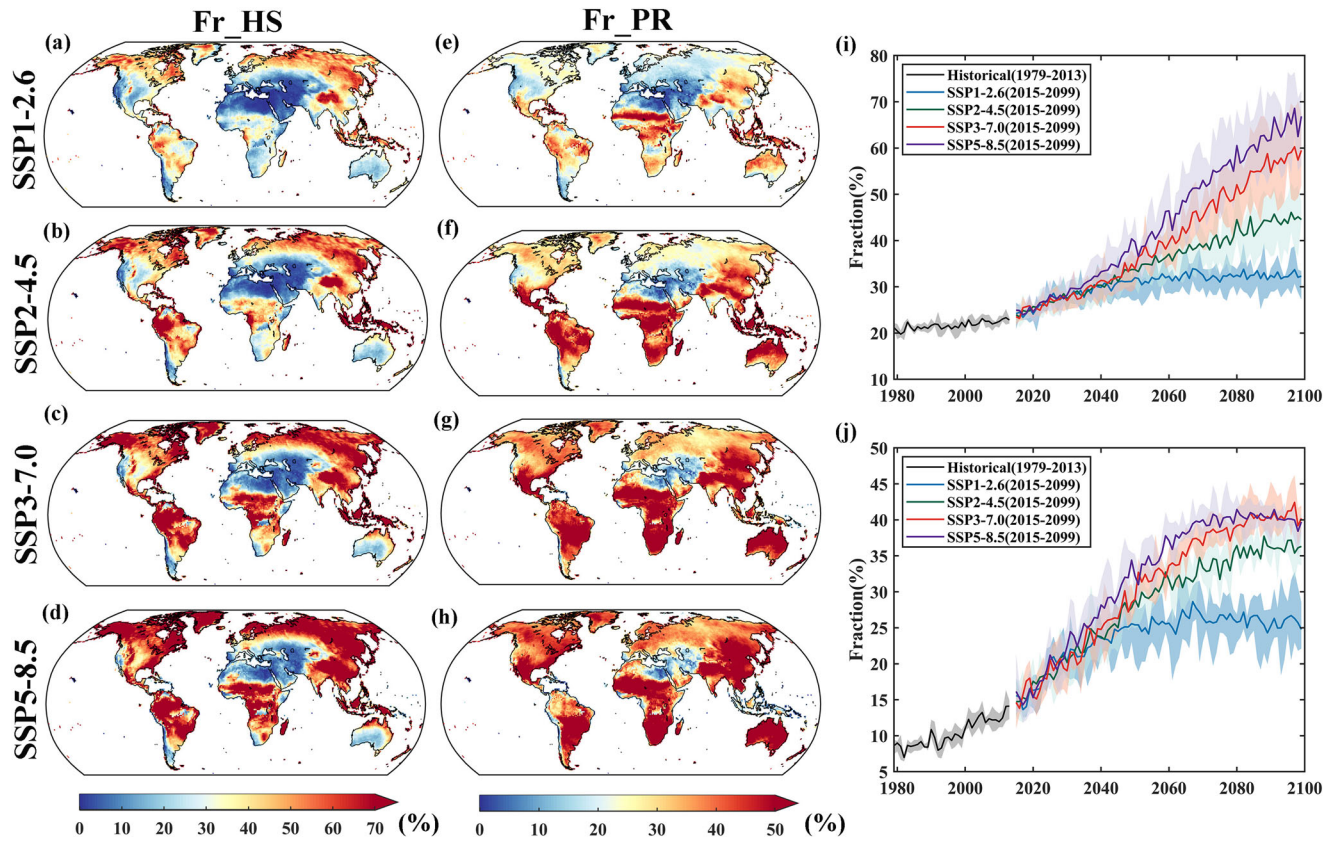


Fig. 2 Projected fraction of CHPE in single extreme events. **a–d** Multi-year average of the fraction of CHPE in HS events in the long-term period (2071–2099) under four scenarios. **e–h** Same as **a–d** but for the fraction of CHPE in PR events. **i** Time series of the fraction of CHPE in HS events for the historical and future periods. **j** Same as **i** but for the fraction of CHPE in PR events.

scenarios for most regions apart from the Mediterranean, the Middle East, and Australia. The Arctic region, central and eastern parts of the United States, northern and eastern regions of South America, the southwestern region of Africa, Qinghai-Tibet Plateau, eastern parts of Asia, and Southeast Asia exhibit larger Fr_{HS} values compared to other regions (Fig. 2a–d), indicating heavy precipitation disaster preventions need to be prepared after experiencing extreme HS conditions. In terms of Fr_{PR} , the annual global average series initially undergoes an increase and then keeps stable across all four scenarios, while the turning point is around 2050 and 2070 under SSP1-2.6 and SSP5-8.5, respectively, and after 2080 under SSP2-4.5 and SSP3-7.0. In the long-term, the global average Fr_{PR} projections surpass 35% under SSP2-4.5, SSP3-7.0, and SSP5-8.5 (Fig. 2j). In southern North America, central South America, central and southern Africa, northern India, southern and northern China, Mongolia, and northern Australia, humid and hot climatic conditions often precede PR events. Fr_{PR} remains low in the Southeastern Mediterranean under all four scenarios (Fig. 2e–h).

Future changes in CHPE characteristics relative to the historical period (1979–2013) are evaluated in terms of their frequency, duration, intensity, and magnitude for the three future sub-periods under four scenarios (Fig. 3 and Supplementary Figs. 5–12). On a global average, the CHPE characteristics are generally projected to increase until the late twenty-first century under SSP2-4.5, SSP3-7.0, SSP5-8.5, and stabilize at around 2050 under SSP1-2.6 (Fig. 3b–e). As the scenarios transition from low-emission scenarios (i.e., SSP1-2.6) to high-emission scenarios (i.e., SSP5-8.5), the global average CHPE characteristics gradually increase, but the differences in characteristics between different scenarios decrease (Fig. 3b–i). This may be because, under higher-emission scenarios,

countries and regions may adopt more emission reduction measures and policies to address the needs of climate change and environmental protection.

CMIP6 multi-model ensemble (MME) projections exhibit an increasing trend in various CHPE characteristics over most land areas, while these increases are much stronger for drought frequency and intensity compared to drought duration and magnitude. The frequency and intensity of CHPE are projected to increase fourfold over half of the global landmasses (Fig. 3a) under high greenhouse gas emission scenarios (i.e., SSP3-7.0 and SSP5-8.5). The largest intensification of CHPE intensity, duration, and magnitude is projected in western and southern North America, northern South America, Mediterranean, central and western Africa, central Asia, southwestern India, Southeast Asia, and northern Australia, while a slightly declining pattern is found in northern Africa in the near-term and under SSP1-2.6. Besides these regions above, the CHPE frequency is projected to increase intensely in southern China. Comparing different scenarios, the differences in the change of CHPE characteristics are more pronounced in the mid-term and long-term periods than in the near-term. These findings suggest that the global land areas will be subject to an escalating risk of CHPE in the medium to long-term future without more aggressive adaptation and mitigation strategies.

Projected changes and drivers in CHPE hazards

We examine changes in the JRP of historical 30-year CHPE within a bivariate framework. In a warming future, we observe a decrease in the JRP of compound extremes across most global regions under all four SSPs, with the decrease becoming more significant

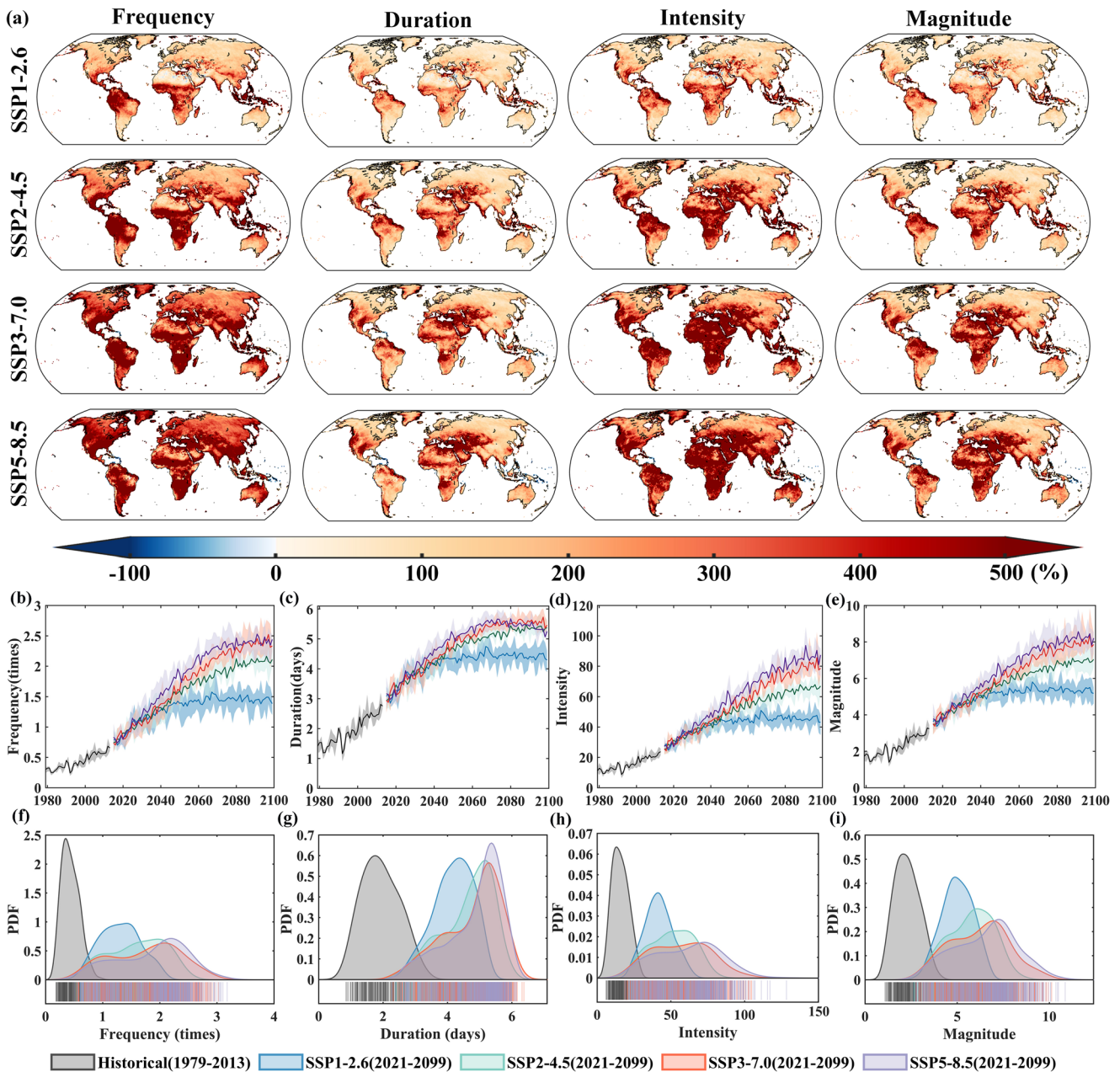
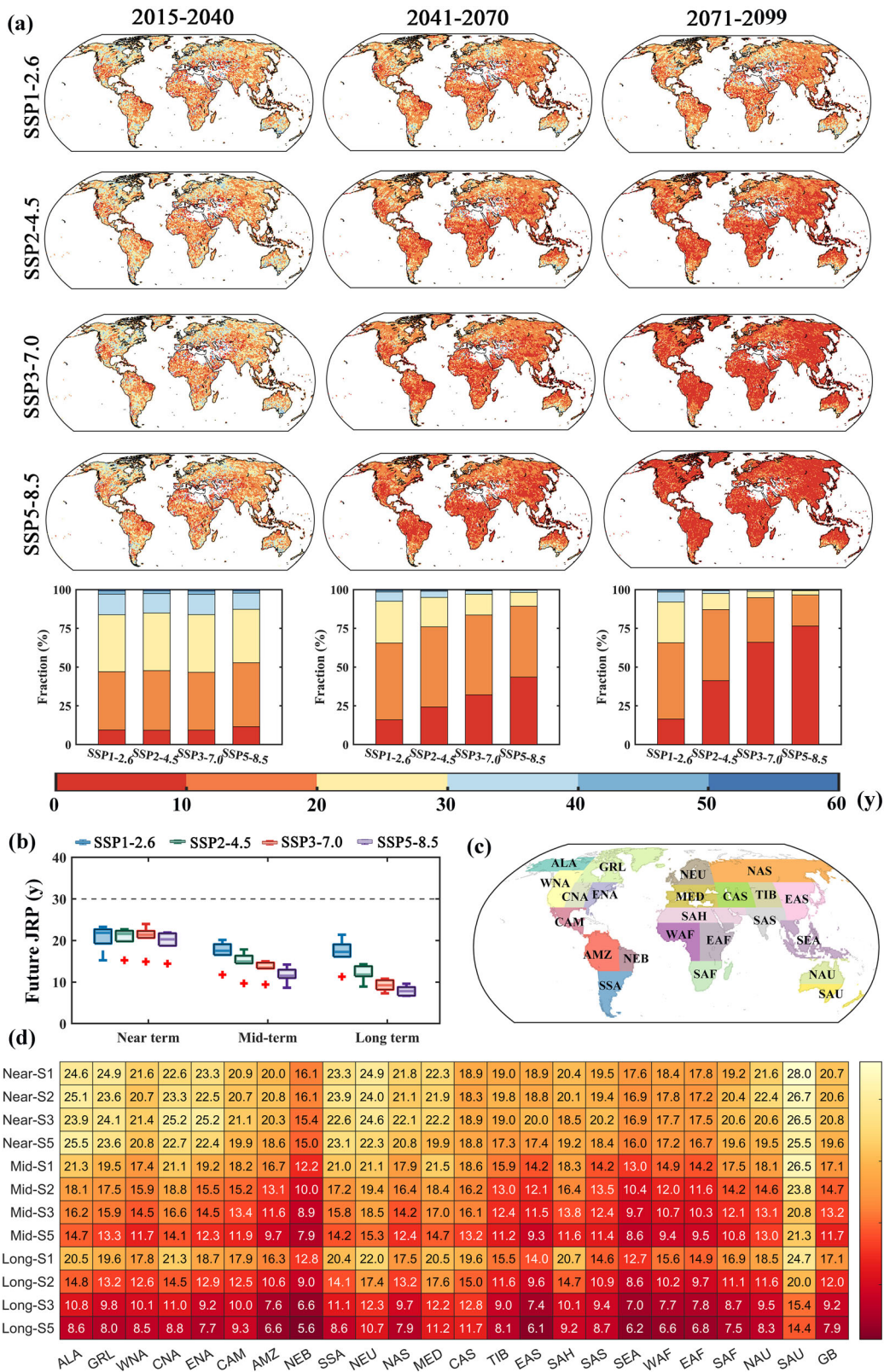


Fig. 3 Future spatiotemporal variations in CHPE characteristics. **a** Spatial features of CHPE characteristics change under diverse future scenarios for the long-term period (2071–2099). **b–e** Annual time series of global average characteristics CHPE events for the historical period (1979–2013) and future period (2015–2099) under four scenarios. The shaded areas denote the interquartile range calculated across the six GCMs. **f–i** Probability density function (PDF) of global annual average drought characteristics for the historical and future period.

from the near-term to the long-term period (Fig. 4a, b). These overall decreases in the JRP occur irrespective of the level of warming but are more pronounced under higher-emission scenarios (i.e., SSP3-7.0 and SSP5-8.5). Furthermore, the disparity among the four scenarios is projected to intensify over time. In particular, the historical 30-year CHPEs are projected to occur more frequently than 10-year over 75 percent of the global land by the long-term under SSP5-8.5. These changes suggest a severe exacerbation of CHPE hazards under global warming. We found high inter-model agreement in the long-term, indicating a highly credible increase in the occurrence of CHPE extremes by the end of this century (Fig. 4b and Supplementary Fig. 13). We also calculate the average future JRP for the 23 regions (Fig. 4c, d). Except for SAU, CAS, MED, and NEU, the average JRPs are

projected to be less than 10 years for other regions in the long-term under SSP5-8.5, and the smallest JRP (around 5–6 years) are found in NEB, EAS, and SEA. The imminent concern is that the occurrence of CHPE extremes for NEB is expected to double in the near-term future.

Changes in the CHPE JRPs can, in principle, be attributed to changes in the marginal distributions of HSs and PRs, as well as the interplay between both hazards^{8,33}. Overall, contributions from HS extremes are the most significant and dominant changes in the JRP of CHPE hazards, followed by contributions from PRs, and the dependence is projected to slightly increase the JRP for most regions (Fig. 5). Specifically, if only the HSs (PRs) changes, the global average JRP is supposed to be ~10 (~25) years (Supplementary Figs. 14–19). In contrast, JRP is projected to



increase over half of the landmass if only the dependence is changed, with a very small disparity among different terms and scenarios. Moreover, we define contribution fraction indicators (i.e., CF_{HS} , CF_{PR} , and CF_C) to quantify the relative contributions of the three drivers (see Methods). We calculate the contribution

fractions separately under four scenarios over the 23 regions (Fig. 5b). Single HS changes account for more than 50 percent of the JRP change across all 23 regions. Single PR changes result in a decrease in all regions except ENA, CAM, NAU under SSP1-2.6, and SAU under both SSP1-2.6 and SSP2-4.5 scenarios. The dependence

Fig. 4 Projected JRP of historical 30-year bivariate CHPEs under diverse future scenarios. **a** Spatial features of future JRP under four scenarios in the near-term (2015–2040), mid-term (2041–2070), and long-term (2071–2099). **b** Global average JRP of historical 30-year bivariate CHPEs. The boxplots represent the spread of JRP estimated from six GCMs. **c** 23 climate regions in global land areas. **d** Heat maps of average JRP for different regions and the global landmass. Near, Mid, and Long in **d** indicates near-term, mid-term, and long-term, respectively. S1, S2, S3, and S5 indicate SSP1-2.6, SSP2-4.5, SSP3-7.0, and SSP5-8.5, respectively. ALA Alaska, GRL Greenland and Northern Territories, WNA Western North America, CNA Central North America, ENA Eastern North America, CAM Central America, AMZ Amazon Basin, NEB Northeastern Brazil, SSA Southern South America, NEU Northern Europe, NAS North Asia, MED Mediterranean Basin, CAS Central Asia, TIB Tibet, EAS East Asia, SAH Sahara, SAS South Asia, SEA Southeast Asia, WAF Western Africa, EAF Eastern Africa, SAF Southern Africa, NAU North Australia, SAU South Australia, GB Global.

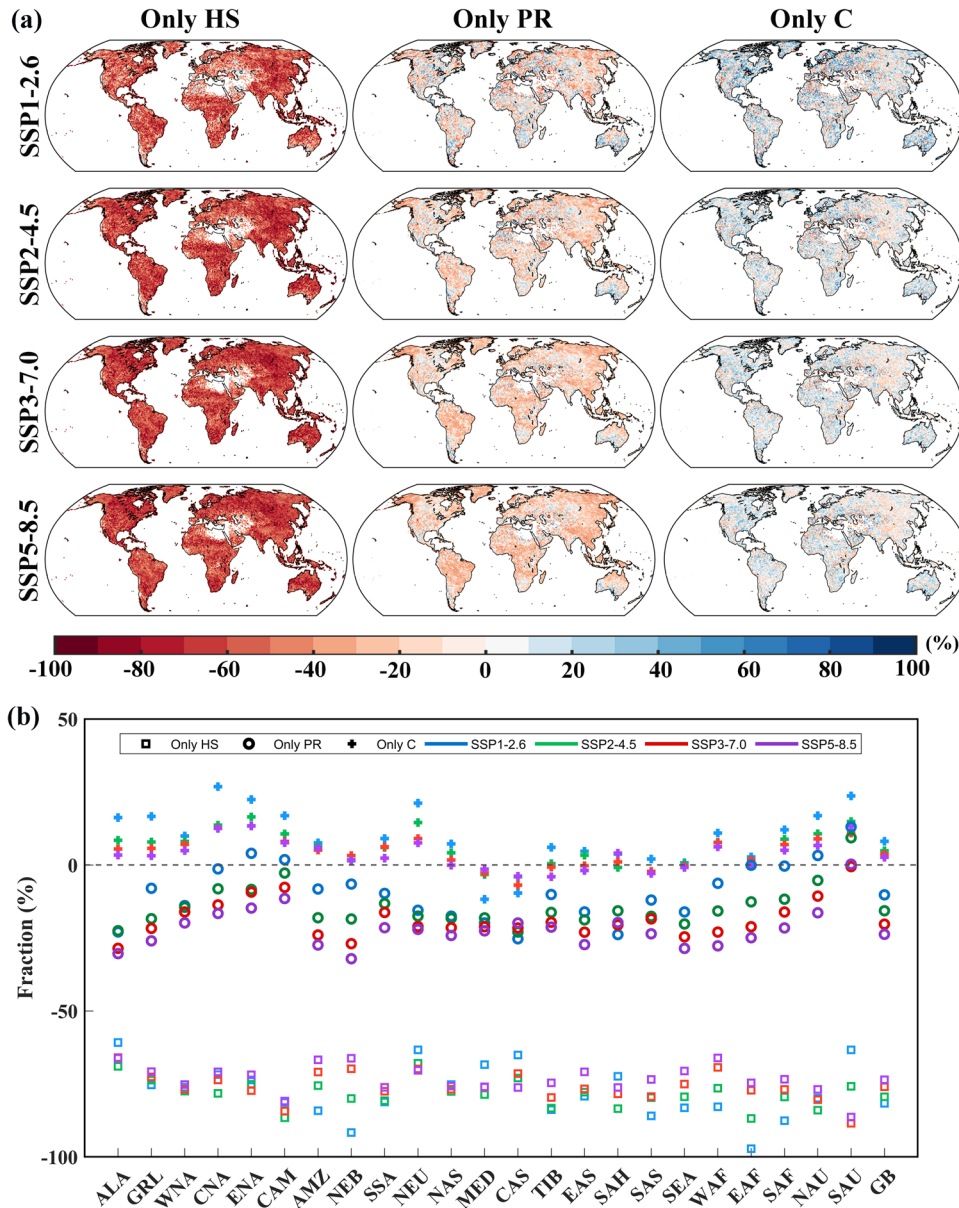


Fig. 5 Projected contribution fraction of three drivers on JRP change of historical 30-year bivariate CHPEs under diverse future scenarios in the long-term (2071–2099). **a** Spatial features of contribution fraction for the three experiments under four scenarios. **b** Average contribution fraction of three drivers of JRP change for different climate regions and the global landmass.

change exhibits a positive contribution to JRP changes in all regions except MED, CAS, TIB, EAS, SAS, and SEA under high-emission scenarios. Comparing the four scenarios, CF_{PR} is larger while CF_C is smaller under higher-emission scenarios for almost all regions. CF_{HS} among different scenarios show two patterns in the

23 regions. For regions with less JRP decrease (e.g., ALA, SAH, SAU, CAS, MED, and NEU), CF_{HS} is significantly smaller under SSP1-2.6 than under other scenarios. However, For regions with a marked decrease in future JRP (e.g., AMZ, NEB, EAS, SEA, WAF, EAF, and SAF), the CF_{HS} is larger under lower emission scenarios.

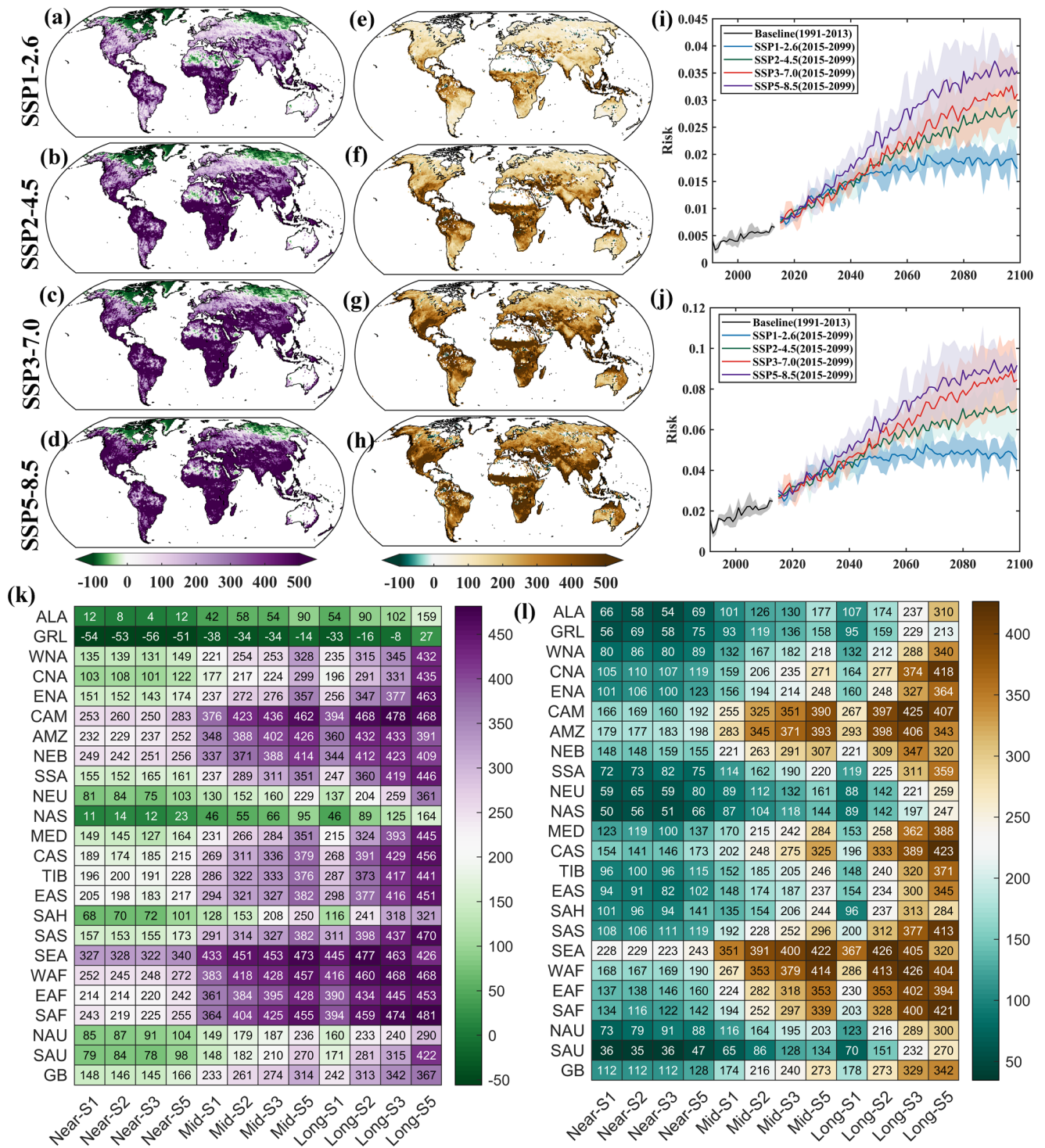


Fig. 6 Projected future risk of CHPE. Projected socioeconomic (a–d, i, k) and ecological risk (e–h, j, l) of CHPE. a–h Spatial maps of risk for the long-term period (2071–2099) under four scenarios. i–j Annual time series of global average CHPE risk. k, l Heat map of average risk changes relative to the baseline period for different regions and the global landmass. Note that the color bars of the spatial maps and the heat maps are different.

Socioeconomic and ecological risk projections of CHPE

Significant increases are found in the future global averages of both socioeconomic risk (SR) and ecological risk (ER) of CHPE relative to the baseline period (Fig. 6; Supplementary Figs. 20 and 21). The specific magnitude of the increase varies depending on the future scenarios considered, with higher-emission scenarios generally

associated with larger risks. Specifically, the future SR sustains a consistent increase before 2060 under all four scenarios and afterward remains at the lowest level under SSP1-2.6 while continuing to enlarge under SSP2-4.5, SSP3-7.0, and SSP5-8.5. The global average ER series under various scenarios exhibits similar patterns to the SR series. The ER series under SSP3-7.0 is closer to

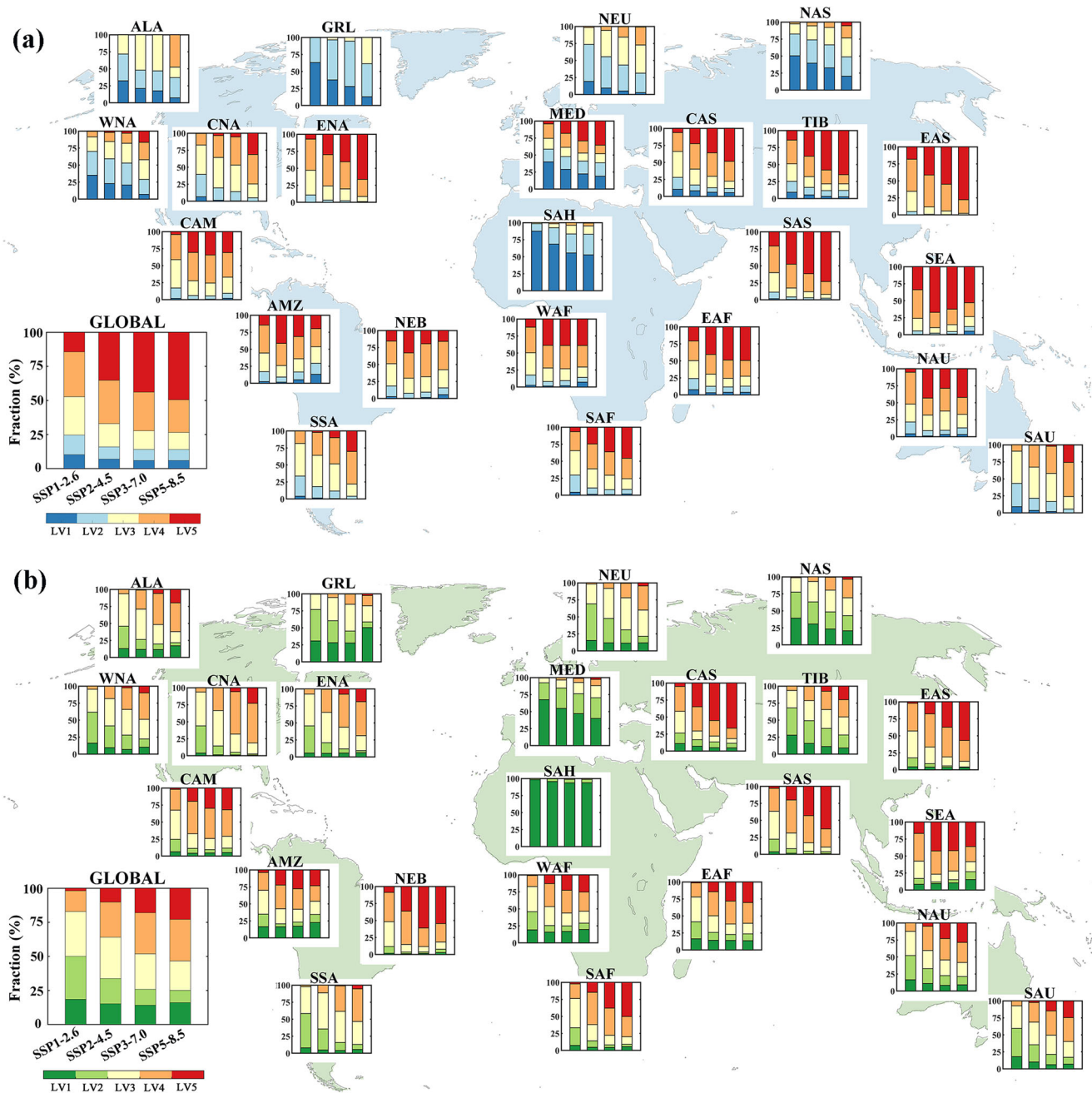


Fig. 7 Social and ecological exposure at different risk levels. Fractions of the exposed population (a) and GPP (b) at five socioeconomic risk levels for each region in the long-term (2071–2099) under four scenarios.

SSP5-8.5 in the second half-century compared to SSP2-4.5, which contrasts with the SR series (Fig. 6i, j). Spatially, the largest increase of SR relative to the baseline period is projected in Central America, coastal areas of northern South America, central South America, western and southeastern Africa, central Asia, western India, southern China, Southeast Asia, and southeastern Australia while the decrease is found in Greenland, northeastern Russia, and Sahara. The largest increase in ER is projected in southeastern North America, northern South America, the Middle East, eastern Africa, southwestern India, northeastern China, Southeast Asia, and northern Australia (Fig. 6a–h). We also calculate the average risk change for the 23 regions (Fig. 6k, l). A large disparity is found in SR change between SSP5-8.5 and other scenarios for WNA, CNA, ENA, NEU, MED, and SAU than other regions in the long-term future, which are

developed regions. For less-developed regions such as CAM, AMZ, NEB, and SEA, the largest increase of SR in the long-term future is projected under SSP3-7.0 rather than SSP5-8.5. The largest projected ER increase is under SSP3-7.0 for CAM, AMZ, NEB, SEA, WAF, and EAF, and under SSP5-8.5 for other regions.

To assess the potential impact of high CHPE risk on socioeconomic and ecological exposure, we classified the raw risk values into five grades using the natural breaks method³⁴ (Supplementary Figs. 22 and 23). The fractions of the exposed population/GDP (Fr_SE) at high SR levels (Levels 4 and 5) indicate that in most regions, under high-emission scenarios in the long-term, approximately 50% of the total population/GDP is exposed to high socioeconomic CHPE risk. Moreover, for regions such as ENA, EAF, TIB, EAS, SAS, and SEA, this fraction exceeds 75% (Fig. 7a). Consistent

with the average risk changes, regions with the largest Fr_SE values under SSP3-7.0 are CAM, AMZ, NEB, and SEA. Similarly, when considering ecological exposure, the fraction of the exposed GPP (Fr_EE) at high ER levels is the highest for SAS, CAS, EAS, SAF, and NEB, which is projected to surpass 75% in the long-term future (Fig. 7 b). The relative magnitudes among the scenarios in terms of Fr_EE are consistent with the average risk changes.

DISCUSSION

In our study, significant increases in future CHPE characteristics are projected compared to the historical period (Figs. 1–3 and Supplementary Figs. 5–8). It's worth noting that there are slight differences in the spatial patterns of CHPE characteristics between the historical (Fig. 1c–f) and near-term periods (Supplementary Figs. 5–8). Take CHPE intensity as an example, large values are found at higher latitudes in the historical period but shift towards lower latitudes in the near-term period. To better understand this discrepancy, we examine spatial maps of CHPE characteristics for each decade from 1979 to 2014 (Supplementary Figs. 24 and 25). We find that regions with high characteristic values shift from areas south of 20°S latitude to the latitude range of 40°N to 20°S. In regions north of 45°N, high-value areas move further northward. In other words, high-value regions tend to shift towards lower latitudes and the Arctic regions during the historical period. The reason may be due to the spatially uneven trends in precipitation^{2,35} and heat stress^{3,36} in different latitudinal zones. Besides, the dependence between HS and PR changes little across distinct zones (Supplementary Fig. 26).

In a warmer future, great values in CHPE characteristics are projected in southern North America, northern and eastern South America, western and central Africa, South Asia, Southeast Asia, and northern Australia. These regions coincide with the main global land monsoon areas, where concurrent rainfall and high temperatures are influenced by warm and humid air from the ocean during summer³⁷. However, it should be noted that northeastern China is likely to witness a smaller increasing trend in CHPE characteristics. One possible explanation may be related to the monsoon season in northeastern China occurs during the winter months, which can result in a cold and dry climate. Additionally, the Arctic region exhibits high CHPE intensity. This is because our definition of CHPE intensity focuses on the magnitude of changes in HS and PR, which are both prominent in the Arctic^{38,39}.

We find that the changes in CHPE hazard are dominated by the increasing HS, which is consistent with previous studies^{8,31,33}. Furthermore, we calculate the contribution fraction of the three drivers for different regions and the global landmass in this study (Fig. 5), which can provide valuable insights into the drivers of future JRP changes and can aid in understanding and mitigating the risks associated with CHPE hazards. Interestingly, we find that the HS contribution is the smallest for regions with less JRP decrease in the future under SSP1-2.6 and for the other regions under SSP5-8.5. This is probably because the contributions of PR change are much larger under higher-emission scenarios in the latter regions with a large decrease in JRP.

Regions with dense populations, particularly highly urbanized areas, are projected to face high socioeconomic risks. The large disparity between SSP5-8.5 and other scenarios found in more developed regions may be due to a more significant increase in population and GDP in these regions than in the less-developed ones under high forcing and traditional development patterns²². Besides, the developing regions such as CAM, AMZ, NEB, and SEA have the largest exposed population and GDP under SSP3-7.0 rather than SSP5-8.5 in the developed regions. This can be attributed to SSP3-7.0 representing an imbalanced and regionally differentiated world, characterized by faster population growth in developing countries with limitations in educational and

technological development. Similarly, the GPP exposed at high ecological risk is the largest under SSP3-7.0 among the four scenarios for CAM, AMZ, NEB, SEA, WAF, and EAF, where uneven development patterns cause more fragile lands.

There are still some limitations in this study. Firstly, there are uncertainties in the data used in the study, including uncertainties in GCMs and multi-mode ensemble approaches. These uncertainties can impact the accuracy and reliability of the results. However, uncertainty exists in all future projection studies and cannot be avoided entirely^{31,40}. In addition, we only consider four typical scenarios in this study while future sustainable development may involve more choices and strategies. Considering a broader range of scenarios and sustainable development pathways can provide a more comprehensive insight. Finally, the risk indicators can be more diverse and comprehensive, and different indicators may result in inconsistent results^{22,41,42}. We only consider the most representative indicators of exposure and vulnerability limited by the large space scale. More comprehensive regional assessments are anticipated to predict CHPE risk by combining more accurate datasets and advanced methods in future work. These limitations suggest areas for improvement in future research, such as using more reliable data, considering additional variables and scenarios, addressing regional differences, and conducting more comprehensive uncertainty analyses to enhance the accuracy and reliability of the study.

METHODS

Datasets

We use reanalysis products to explore the historical CHPE and atmospheric conditions. The daily $1^\circ \times 1^\circ$ 2 m air temperature, 2 m dewpoint temperature, SSHF, CAPE, VIMC, and TCWV from ERA5 for the 1979–2014 period are utilized in this study. The daily $0.5^\circ \times 0.5^\circ$ precipitation from the Climate Prediction Center (CPC) for the 1979–2014 period is used and resampled to $1^\circ \times 1^\circ$.

To project future climatic conditions, we select a multi-model ensemble including six CMIP6 GCMs (i.e., CNRM-CM6-1, EC-Earth3-Veg, KACE-1-0-G, MPI-ESM1-2-HR, MRI-ESM2-0, NorESM2-MM), of which the mean equilibrium climate sensitivity is 3.71, falling within the always maintained range of 1.5–4.5 °C⁴³. Details of the selected GCMs are shown in Supplementary Table 1. We download daily variables of precipitation, 2 m air temperature, relative humidity, and monthly GPP for the historical (1979–2014) periods and the future (2015–2100) periods. Projections under four future combined scenarios are employed, i.e., SSP1-2.6 (+2.6 W m⁻²; low forcing sustainability pathway), SSP2-4.5 (+4.5 W m⁻²; medium forcing middle of the road pathway), SSP3-7.0 (+7.0 W m⁻²; medium to high forcing regional rivalry pathway), and SSP5-8.5 (+8.5 W m⁻²; high forcing fossil-fueled development pathway). A common bilinear interpolation scheme is applied to interpolate the meteorological variables to a common spatial resolution of $1^\circ \times 1^\circ$ ^{8,44,45}. We adopt the widely used Quantile Mapping (QM) method^{31,46–48} to correct the daily precipitation and calculated T_h .

To analyze the socioeconomic and ecological risk of CHPE, a variety of datasets are used in this study. We use global population data from the Global Rural-Urban Mapping Project, Version 1 (1990, 1995, and 2000) and WorldPop (2000–2014) with a resolution of 1 km^{49,50}. Gridded GDP data with a spatial resolution of 5 arc-min for the 1991–2014 period are employed⁵¹. To project future global exposure of population and assets to CHPE, we use global $0.5^\circ \times 0.5^\circ$ population and GDP projections under the four SSP scenarios^{52–54}. $0.25^\circ \times 0.25^\circ$ GPP data used to calculate the ecological exposure for the 1988–2014 period are from the VODCA2GPP dataset⁵⁵. Historical land cover data are gained from the European Space Agency with a 300-m spatial resolution. Global land cover projections with a $0.1^\circ \times 0.1^\circ$ resolution for

2020–2100 under different RCP scenarios⁵⁶ are utilized. All the above data are uniformed to $1^\circ \times 1^\circ$ resolution.

Definition and characterization of CHPEs on a grid cell

The CHPEs refer to the occurrence of HS events followed by PR events within a prescribed temporal interval. It should be noted that we only consider the sequential occurrence of PR following the termination of the HS event, ignoring the concurrent PR and HS events. In this study, we particularly focus on the warm season, which is defined as the hottest five months using ERA5 temperature climatology (Supplementary Fig. 2). We calculate T_h based on the widely used formula of wet bulb temperature T_{WB} ^{57,58}.

$$T_h = T_{WB} + 4.5 \left(1 - \left[\frac{RH}{100} \right]^2 \right) \quad (1)$$

$$T_{WB} = T \times \text{atan} \left[0.151977 \times (RH + 8.313659)^{\frac{1}{2}} \right] + \text{atan}(T + RH) - \text{atan}(RH - 1.676331) + 0.00391838 \times RH^{1.5} \times \text{atan}(0.023101 \times RH) - 4.686035 \quad (2)$$

$$RH = 100 \times \exp \left[-\frac{L}{R_w(T + 273.15)T_d} (T - T_d) \right] \quad (3)$$

$$SH = \frac{RH}{100} \times \frac{es(T)}{R_w(T + 273.15)} \quad (4)$$

where atan is the arc tangent, T is the dry air temperature ($^\circ\text{C}$), T_{WB} is the wet bulb temperature ($^\circ\text{C}$), T_h is the lethal heat stress temperature ($^\circ\text{C}$), T_d is the dewpoint temperature in Kelvin, RH is the near-surface relative humidity (%), SH is the near-surface specific humidity (g m^{-3}), $es(T)$ is the saturated water vapor pressure at T , L is the enthalpy of vaporization ($2.472 \times 10^6 \text{ J kg}^{-1}$), R_w is the gas constant for water vapor ($461.5 \text{ J K}^{-1} \text{ kg}^{-1}$).

For each grid, a single HS event (orange slashed area in Fig. 8) is defined when the daily T_h exceeds its 90th percentile in the warm season over 1979–2014 for at least three consecutive days. A single PR event (blue slashed area in Fig. 8) is detected when daily precipitation is higher than its 90th percentile on wet days from 1979–2014. We use the 90th percentile to capture an adequate number of compound events for analysis. The percentile-based thresholds for identifying extreme events have been proven reasonable in previous studies^{3,33,59}. Accordingly, we define a CHPE as an HS event followed by a PR event within 3 days (the 3-day period refers to before the onset of the PR event and after the cessation of the HS event). To avoid redundancy, we matched each PR event with the nearest HS event and only retained the

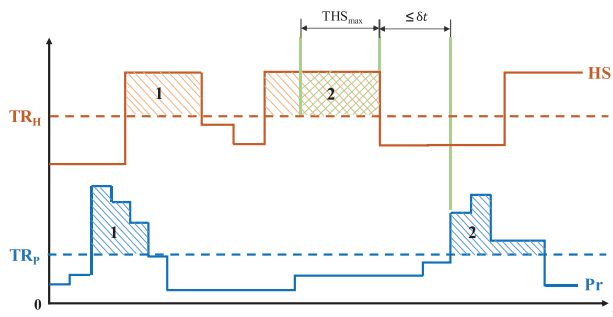


Fig. 8 Schema of the CHPE identification. TR_H and TR_P are the thresholds of the heat stress (HS) and precipitation (PR) series. The δt is the max time span between an HS event and the followed PR event and THS_{max} is the max limit duration of an HS event in CHPE.

largest PR event accompanied by the same HS event. Finally, we set the max duration of the HS event (THS_{max}) in CHPEs (green slashed area in Fig. 8) to 7 days from the last day forward, since the physical connection may weaken if the time interval between HS and PR events is too long. The CHPEs are characterized by four metrics: frequency, defined as the number of CHPEs in a year; duration, defined as the total number of days in the HS and PR event. For CHPE intensity and magnitude, we combine the normalized daily anomalies in HS and PR:

$$IS_{HS} = \sum_{d=1}^{DU_{HS}} \left(\frac{T_{hd} - T_{h25p}}{T_{h75p} - T_{h25p}} \right), IS_{PR} = \sum_{d=1}^{DU_{PR}} \left(\frac{Pr_d - Pr_{25p}}{Pr_{75p} - Pr_{25p}} \right), IS_C = IS_{HS} \times IS_{PR} \quad (5)$$

$$MD_{HS} = \frac{\sum_{d=1}^{DU_{HS}} \left(\frac{T_{hd} - T_{h25p}}{T_{h75p} - T_{h25p}} \right)}{DU_{HS}}, MD_{PR} = \frac{\sum_{d=1}^{DU_{PR}} \left(\frac{Pr_d - Pr_{25p}}{Pr_{75p} - Pr_{25p}} \right)}{DU_{PR}}, MD_C = MD_{HS} \times MD_{PR} \quad (6)$$

where T_{hd} and Pr_d are the heat stress temperature and precipitation in day d , respectively. T_{h25p} and T_{h75p} are the 25th and 75th percentile of T_h in the warm season over 1991–2014, respectively. Pr_{25p} and Pr_{75p} are the 25th and 75th percentile of daily precipitation in wet days over 1991–2014, respectively. IS_{HS} and IS_{PR} are the intensity of HS and PR events in CHPE, respectively. MD_{HS} and MD_{PR} are the magnitudes of HS and PR events in CHPE, respectively.

Quantile Mapping method

The QM method is used to correct and minimize systematic biases in daily precipitation, temperature, and relative humidity from the six CMIP6 GCMs. The calibration results are provided in Supplementary Fig. 27. The general mechanism of the QM method is to find a transfer function to achieve the best fit that maps the simulated cumulative distribution function (CDF) of the variables to the observed CDF. The transfer function can be described as follows:

$$x_{bc}(t) = F_{o,h}^{-1} \{ F_{m,h} [x_{m,f}(t)] \} \quad (7)$$

where $x_{bc}(t)$ is the bias-corrected value, $x_{m,f}(t)$ is the model output in the future period at time t , $F_{o,h}^{-1}$ and $F_{m,h}$ mean the inverse CDF for historical observation and model simulation series, respectively.

Bivariate return period variation and attribution

To evaluate the joint comprehensive impacts of extreme HS and PR on CHPEs, we employ copulas to analyze bivariate return periods. We initially estimate the marginal distributions of HS and PR by utilizing five candidate parametric distributions (i.e., Gamma, GEV, Weibull, Normal, and Log-normal). Subsequently, we employed five commonly used bivariate copulas (Gaussian copula, Student's t copula, Frank copula, Clayton copula, and Gumbel copula) to link the marginal distributions of HSs and PRs. The selection of the best-fitting marginal distributions and copulas is based on the smallest Akaike information criterion (AIC)⁶⁰. We employ the “and” criterion of the joint return period (JRP) to measure the bivariate hazards of CHPE:

$$JRP = \frac{E}{1 - F(IS_{HS}) - F(IS_{PR}) + C(F(IS_{HS}), F(IS_{PR}))} \quad (8)$$

where $F(IS_{HS})$ ($F(IS_{PR})$) is the marginal cumulative distribution of the IS_{HS} (IS_{PR}), respectively, and $C(F(IS_{HS}), F(IS_{PR}))$ represents the joint distribution of $F(IS_{HS})$ and $F(IS_{PR})$. In accordance with previous studies^{8,61,62}, we set the same exceedance probability for both the HS and PR extremes: $F(IS_{HS}) = F(IS_{PR})$. E denotes the average inter-arrival time between compound events.

Table 1. Socioeconomic/ecological risk assessment indicators.

	W1 ^a	Indicators (correlation)	W2 ^a	W1 × W2
Hazard	1/2	CHPE frequency (+)	1/3	1/6
		CHPE duration (+)	1/3	1/6
		CHPE intensity (+)	1/3	1/6
Exposure-S	1/4	Population density (+)	1/2	1/8
		GDP density (+)	1/2	1/8
Vulnerability-S	1/4	Ratio of the cropland and built-up land (+)	1/2	1/8
		GDP per capita (-)	1/2	1/8
Exposure-E	1/4	GPP (+)	1	1/4
Vulnerability-E	1/4	Ratio of the scrub, grass, wetlands and cropland (+)	1	1/4

^aW1 is the weight of hazard, exposure, and vulnerability (Eq. 10); W2 is the weight of each indicator (Eq. 11). +/- represents the positive/negative correlation between the indicator and risk.

Given the potential changes in future CHPE hazards in a warmer climate, we individually construct individual bivariate distributions in the historical (1979–2014) and three future periods (Near-term: 2015–2040; Mid-term: 2041–2070; Long-term: 2071–2099). To further understand the factors driving changes in JRP, we also carry out three separate experiments to disentangle the relative contributions of three drivers (i.e., HS, PR, and their dependence) to variations in CHPE hazards as suggested by previous studies^{8,33,63}: (1) fixing the $F(IS_{HS})$ and $C(F(IS_{HS}), F(IS_{PR}))$ in the historical period and exchanging the $F(IS_{PR})$ in the future period; (2) fixing the $F(IS_{PR})$ and $C(F(IS_{HS}), F(IS_{PR}))$ in the historical period and exchanging the $F(IS_{HS})$ in the future period; and (3) fixing both $F(IS_{HS})$ and $F(IS_{PR})$ in the historical period and using $C(F(IS_{HS}), F(IS_{PR}))$ for the future period (more details see Supplementary Methods). Then we define the contribution fraction of the three drivers:

$$CF_x = \frac{\Delta JRP_x}{\text{abs}(\Delta JRP_{HS}) + \text{abs}(\Delta JRP_{PR}) + \text{abs}(\Delta JRP_C)} \quad (9)$$

where CF_x and ΔJRP_x represent the contribution fraction and change of JRP result from driver x , respectively.

Socioeconomic and ecological risk calculation

CHPE risk is assessed through indicators of three determinants: hazard, exposure, and vulnerability. The selected indicators are listed in Table 1. In this study, we separately calculate the socioeconomic risk (SR) and ecological risk (ER) of CHPE using the formulation implemented by the United Nations International Strategy for Disaster Reduction (UNISDR)⁶⁴, which has been widely applied in previous risk studies^{65–67}. We set the weight of the inflector (hazard) to 0.5 and the weight of the acceptor (exposure and vulnerability) to 0.25 each²².

$$\text{Risk} = \text{Hazard}^{0.5} \times \text{Exposure}^{0.25} \times \text{Vulnerability}^{0.25} \quad (10)$$

$$T = \prod_{i=1}^n Z_i^{w_i} \quad (11)$$

where T refers to hazard, exposure, and vulnerability, n is the number of indicators in T , Z_i is the indicator and w_i is the weight of it.

A linear scale normalization is performed to standardize all raw indicator values to an identical range of 0 to 1.

$$\begin{cases} Z_i = \frac{X_i - X_{\min}}{X_{\max} - X_{\min}} \times 10 \text{ positive correlation} \\ Z_i = \left(1 - \frac{X_i - X_{\min}}{X_{\max} - X_{\min}}\right) \times 10 \text{ negative correlation} \end{cases} \quad (12)$$

where Z_i and X_i represent the normalized and raw indicator values for grid i , respectively, X_{\max} and X_{\min} represent the maximum and minimum values across all grids, respectively.

DATA AVAILABILITY

The GCM data can be accessed from the CMIP6 archive (<https://esgf-node.lln.gov/projects/cmip6/>). The ERA5 data can be accessed from <https://cds.climate.copernicus.eu/#/home>. The daily $0.5^\circ \times 0.5^\circ$ precipitation from the Climate Prediction Center (CPC) for the 1979–2014 period is from <https://www.cpc.ncep.noaa.gov/>. Global annual 1 km population data from the WorldPop archive can be obtained at <https://www.worldpop.org/geodata/listing?id=64>. Global 1 km population data in 1990, 1995, and 2000 can be accessed from the Socioeconomic Data and Applications Center (SEDAC) (<https://sedac.ciesin.columbia.edu/data/collection/grump-v1>). Global annual 5 arc-min GDP data from 1991 to 2014 can be accessed from Dryad Data (<https://datadryad.org/stash/dataset/doi:10.5061/dryad.dk1j0>). Projected 0.5° gridded global population and GDP data can be accessed from the Science Data Bank (<https://www.scidb.cn/en/detail?dataSetId=73c1ddb79e54638bd0ca2a6bd48e3ff>). Global annual 300 m land cover data from 1991 to 2014 can be gained from the European Space Agency (ESA, <https://www.esa-landcover-cci.org/?q=node/197>). Projected land cover data are gained from Fan et al.⁵⁶ under a data sharing agreement, and the authors are not authorized to redistribute the data.

CODE AVAILABILITY

The MATLAB codes for data processing are available at <https://github.com/Zhilong-ZHOU/npj01816>. Any requests for code or data can be directed to the authors.

Received: 9 October 2023; Accepted: 18 January 2024;
Published online: 31 January 2024

REFERENCES

- Blöschl, G. et al. Current European flood-rich period exceptional compared with past 500 years. *Nature* **583**, 560–566 (2020).
- Papalexidou, S. M. & Montanari, A. Global and regional increase of precipitation extremes under global warming. *Water Resour. Res.* **55**, 4901–4914 (2019).
- Perkins-Kirkpatrick, S. E. & Lewis, S. C. Increasing trends in regional heatwaves. *Nat. Commun.* **11**, 3357 (2020).
- Zhang, W. & Villarini, G. Deadly compound heat stress-flooding hazard across the Central United States. *Geophys. Res. Lett.* **47**, e2020GL089185 (2020).
- Konapala, G., Mishra, A. K., Wada, Y. & Mann, M. E. Climate change will affect global water availability through compounding changes in seasonal precipitation and evaporation. *Nat. Commun.* **11**, 3044 (2020).
- Zscheischler, J. et al. A typology of compound weather and climate events. *Nat. Rev. Earth Environ.* **1**, 333–347 (2020).
- Ren, J., Huang, G., Zhou, X. & Li, Y. Downscaled compound heatwave and heavy-precipitation analyses for Guangdong, China in the twenty-first century. *Clim. Dyn.* **61**, 2885–2905 (2023).
- Gu, L. et al. Global increases in compound flood-hot extreme hazards under climate warming. *Geophys. Res. Lett.* **49**, e2022GL097726 (2022).
- You, J. & Wang, S. Higher probability of occurrence of hotter and shorter heat waves followed by heavy rainfall. *Geophys. Res. Lett.* **48**, e2021GL094831 (2021).
- Ning, G. et al. Rising risks of compound extreme heat-precipitation events in China. *Int. J. Climatol.* **42**, 5785–5795 (2022).
- Zscheischler, J. et al. Future climate risk from compound events. *Nat. Clim. Change* **8**, 469–477 (2018).
- Mora, C. et al. Global risk of deadly heat. *Nat. Clim. Change* **7**, 501–506 (2017).
- Buzan, J. R. & Huber, M. Moist heat stress on a hotter earth. *Annu. Rev. Earth Planet. Sci.* **48**, 623–655 (2020).
- Zhao, Y., Ducharme, A., Sultan, B., Braconnot, P. & Vautard, R. Estimating heat stress from climate-based indicators: present-day biases and future spreads in the CMIP5 global climate model ensemble. *Environ. Res. Lett.* **10**, 084013 (2015).
- Kent, S. T., McClure, L. A., Zaitchik, B. F., Smith, T. T. & Gohlke, J. M. Heat waves and health outcomes in Alabama (USA): the importance of heat wave definition. *Environ. Health Perspect.* **122**, 151–158 (2014).
- Heo, S. & Bell, M. L. Heat waves in South Korea: differences of heat wave characteristics by thermal indices. *J. Expo. Sci. Environ. Epidemiol.* **29**, 790–805 (2019).

17. Speizer, S., Raymond, C., Ivanovich, C. & Horton, R. M. Concentrated and intensifying humid heat extremes in the IPCC AR6 regions. *Geophys. Res. Lett.* **49**, e2021GL097261 (2022).
18. Kong, Q. & Huber, M. Explicit calculations of wet-bulb globe temperature compared with approximations and why it matters for labor productivity. *Earth's Future* **10**, e2021EF002334 (2022).
19. Schwingshackl, C., Sillmann, J., Vicedo-Cabrera, A. M., Sandstad, M. & Aunan, K. Heat stress indicators in CMIP6: estimating future trends and exceedances of impact-relevant thresholds. *Earth's Future* **9**, e2020EF001885 (2021).
20. Wouters, H. et al. Soil drought can mitigate deadly heat stress thanks to a reduction of air humidity. *Sci. Adv.* **8**, eabe6653 (2022).
21. IPCC. *Managing the Risks of Extreme Events and Disasters to Advance Climate Change Adaptation: Special Report of the Intergovernmental Panel on Climate Change*. Vol. 1 (Cambridge University Press, 2012).
22. Zhou, Z. et al. Projecting global drought risk under various SSP-RCP scenarios. *Earth's Future* **11**, e2022EF003420 (2023).
23. Tellman, B. et al. Satellite imaging reveals increased proportion of population exposed to floods. *Nature* **596**, 80–86 (2021).
24. Jiang, R. et al. Substantial increase in future fluvial flood risk projected in China's major urban agglomerations. *Commun. Earth Environ.* **4**, 1–11 (2023).
25. Brown, P. T. et al. Climate warming increases extreme daily wildfire growth risk in California. *Nature* **621**, 760–766 (2023).
26. Meza, I. et al. Global-scale drought risk assessment for agricultural systems. *Nat. Hazards Earth Syst. Sci.* **20**, 695–712 (2020).
27. Flach, M. et al. Vegetation modulates the impact of climate extremes on gross primary production. *Biogeosciences* **18**, 39–53 (2021).
28. Shao, H. et al. Impacts of climate extremes on ecosystem metrics in southwest China. *Sci. Total Environ.* **776**, 145979 (2021).
29. Krause, A. et al. Quantifying the impacts of land cover change on gross primary productivity globally. *Sci. Rep.* **12**, 18398 (2022).
30. O'Neill, B. C. et al. The Scenario Model Intercomparison Project (ScenarioMIP) for CMIP6. *Geosci. Model Dev.* **9**, 3461–3482 (2016).
31. Zhang, Q. et al. High sensitivity of compound drought and heatwave events to global warming in the future. *Earth's Future* **10**, e2022EF002833 (2022).
32. Raymond, C. et al. Understanding and managing connected extreme events. *Nat. Clim. Change* **10**, 611–621 (2020).
33. Yin, J. et al. Future socio-ecosystem productivity threatened by compound drought–heatwave events. *Nat. Sustain.* **6**, 259–272 (2023).
34. Jiang, B. Head/tail breaks: a new classification scheme for data with a heavy-tailed distribution. *Prof. Geogr.* **65**, 482–494 (2013).
35. Adler, R. F., Gu, G., Sapiiano, M., Wang, J.-J. & Huffman, G. J. Global precipitation: means, variations and trends during the satellite era (1979–2014). *Surv. Geophys.* **38**, 679–699 (2017).
36. Chen, X. et al. Changes in global and regional characteristics of heat stress waves in the 21st century. *Earth's Future* **8**, e2020EF001636 (2020).
37. Chang, M. et al. Understanding future increases in precipitation extremes in global land monsoon regions. *J. Clim.* **35**, 1839–1851 (2022).
38. McCrystall, M. R., Stroeve, J., Serreze, M., Forbes, B. C. & Screen, J. A. New climate models reveal faster and larger increases in Arctic precipitation than previously projected. *Nat. Commun.* **12**, 6765 (2021).
39. Rantanen, M. et al. The Arctic has warmed nearly four times faster than the globe since 1979. *Commun. Earth Environ.* **3**, 1–10 (2022).
40. Yin, Q., Wang, J., Ren, Z., Li, J. & Guo, Y. Mapping the increased minimum mortality temperatures in the context of global climate change. *Nat. Commun.* **10**, 4640 (2019).
41. Sutton, R. T. Climate science needs to take risk assessment much more seriously. *Bull. Am. Meteorol. Soc.* **100**, 1637–1642 (2019).
42. Zhao, D., Zhang, Z. & Zhang, Y. Soil moisture dominates the forest productivity decline during the 2022 China compound drought-heatwave event. *Geophys. Res. Lett.* **50**, e2023GL104539 (2023).
43. Schlund, M., Lauer, A., Gentine, P., Sherwood, S. C. & Eyring, V. Emergent constraints on equilibrium climate sensitivity in CMIP5: do they hold for CMIP6? *Earth Syst. Dyn.* **11**, 1233–1258 (2020).
44. Kim, Y.-H., Min, S.-K., Zhang, X., Sillmann, J. & Sandstad, M. Evaluation of the CMIP6 multi-model ensemble for climate extreme indices. *Weather Clim. Extrem.* **29**, 100269 (2020).
45. Li, Z., Liu, T., Huang, Y., Peng, J. & Ling, Y. Evaluation of the CMIP6 Precipitation Simulations Over Global Land. *Earth's Future* **10**, e2021EF002500 (2022).
46. Cannon, A. J. Multivariate quantile mapping bias correction: an N-dimensional probability density function transform for climate model simulations of multiple variables. *Clim. Dyn.* **50**, 31–49 (2018).
47. Olschewski, P. et al. An ensemble-based assessment of bias adjustment performance, changes in hydrometeorological predictors and compound extreme events in EAS-CORDEX. *Weather Clim. Extrem.* **39**, 100531 (2023).
48. Poppick, A. & McKinnon, K. A. Observation-based simulations of humidity and temperature using quantile regression. *J. Clim.* **33**, 10691–10706 (2020).
49. Balk, D. L. et al. Determining global population distribution: methods, applications and data. In: *Advances in Parasitology* (eds. Hay, S. I., Graham, A. & Rogers, D. J.) Vol. 62, 119–156 (Academic Press, 2006).
50. Lloyd, C. T. et al. Global spatio-temporally harmonised datasets for producing high-resolution gridded population distribution datasets. *Big Earth Data* **3**, 108–139 (2019).
51. Kumm, M., Taka, M. & Guillaume, J. H. A. Gridded global datasets for Gross Domestic Product and Human Development Index over 1990–2015. *Sci. Data* **5**, 20004 (2018).
52. Huang, J. et al. Effect of fertility policy changes on the population structure and economy of China: from the perspective of the shared socioeconomic pathways. *Earth's Future* **7**, 250–265 (2019).
53. Jing, C. et al. Population, urbanization and economic scenarios over the Belt and Road region under the Shared Socioeconomic. *Pathw. J. Geogr. Sci.* **30**, 68–84 (2020).
54. Mondal, S. K. et al. Doubling of the population exposed to drought over South Asia: CMIP6 multi-model-based analysis. *Sci. Total Environ.* **771**, 145186 (2021).
55. Wild, B. et al. VODCA2GPP—a new, global, long-term (1988–2020) gross primary production dataset from microwave remote sensing. *Earth Syst. Sci. Data* **14**, 1063–1085 (2022).
56. Fan, Z., Bai, R. & Yue, T. Scenarios of land cover in Eurasia under climate change. *J. Geogr. Sci.* **30**, 3–17 (2020).
57. Stull, R. Wet-bulb temperature from relative humidity and air temperature. *J. Appl. Meteorol. Climatol.* **50**, 2267–2269 (2011).
58. Yin, J. et al. Global increases in lethal compound heat stress: hydrological drought hazards under climate change. *Geophys. Res. Lett.* **49**, e2022GL100880 (2022).
59. Zhou, S., Yu, B. & Zhang, Y. Global concurrent climate extremes exacerbated by anthropogenic climate change. *Sci. Adv.* **9**, eabo1638 (2023).
60. Akaike, H. A new look at the statistical model identification. *IEEE Trans. Autom. Control* **19**, 716–723 (1974).
61. Zhou, S. et al. Land–atmosphere feedbacks exacerbate concurrent soil drought and atmospheric aridity. *Proc. Natl Acad. Sci. USA* **116**, 18848–18853 (2019).
62. Zscheischler, J. & Seneviratne, S. I. Dependence of drivers affects risks associated with compound events. *Sci. Adv.* **3**, e1700263 (2017).
63. Bevacqua, E. et al. Higher probability of compound flooding from precipitation and storm surge in Europe under anthropogenic climate change. *Sci. Adv.* **5**, eaaw5531 (2019).
64. Pearson, L. & Pelling, M. The UN Sendai Framework for Disaster Risk Reduction 2015–2030: negotiation process and prospects for science and practice. *J. Extrem. Events* **02**, 1571001 (2015).
65. Carrão, H., Naumann, G. & Barbosa, P. Mapping global patterns of drought risk: an empirical framework based on sub-national estimates of hazard, exposure and vulnerability. *Glob. Environ. Change* **39**, 108–124 (2016).
66. Liu, Y. & Chen, J. Future global socioeconomic risk to droughts based on estimates of hazard, exposure, and vulnerability in a changing climate. *Sci. Total Environ.* **751**, 142159 (2021).
67. Su, B. et al. Drought losses in China might double between the 1.5 °C and 2.0 °C warming. *Proc. Natl Acad. Sci. USA* **115**, 10600–10605 (2018).

ACKNOWLEDGEMENTS

This work was supported by the National Natural Science Foundation of China (52279023). We also acknowledge support from the National Natural Science Foundation of China (41890824) and the National Key Research and Development Program of China (2017YFA0603704).

AUTHOR CONTRIBUTIONS

L.Z. and Z.Z. designed the research. Z.Z. and C.H. defined the details of the framework for this study. Z.Z. conducted all analyses and wrote the first draft of the manuscript. All authors worked together on the interpretation of the results and writing of the final manuscript.

COMPETING INTERESTS

The authors declare no competing interests.

ADDITIONAL INFORMATION

Supplementary information The online version contains supplementary material available at <https://doi.org/10.1038/s41612-024-00579-4>.

Correspondence and requests for materials should be addressed to Liping Zhang or Chen Hu.

Reprints and permission information is available at <http://www.nature.com/reprints>

Publisher's note Springer Nature remains neutral with regard to jurisdictional claims in published maps and institutional affiliations.



Open Access This article is licensed under a Creative Commons Attribution 4.0 International License, which permits use, sharing, adaptation, distribution and reproduction in any medium or format, as long as you give appropriate credit to the original author(s) and the source, provide a link to the Creative Commons license, and indicate if changes were made. The images or other third party material in this article are included in the article's Creative Commons license, unless indicated otherwise in a credit line to the material. If material is not included in the article's Creative Commons license and your intended use is not permitted by statutory regulation or exceeds the permitted use, you will need to obtain permission directly from the copyright holder. To view a copy of this license, visit <http://creativecommons.org/licenses/by/4.0/>.

© The Author(s) 2024